

Metal-insulator-metal nanorod arrays for subwavelength imaging

Xiaofei Wu, Jiasen Zhang*, and Qihuang Gong

State Key Laboratory for Mesoscopic physics and Department of Physics,
Peking University, Beijing 100871, P. R. China

*Corresponding author: jszhang@pku.edu.cn

Abstract: We proposed using metal-insulator-metal (MIM) nanorod arrays for subwavelength imaging to improve the resolution based on the notable ability of field confinement of the MIM nanorods. The field distribution of a single Au-SiO₂-Au nanorod, coupling between two nanorods and image transfer of shaped dipole sources through nanorod arrays were investigated by using the finite-difference time-domain method and compared with the case of Au nanorods. A resolution limit of $\sim\lambda/20$ of the Au-SiO₂-Au nanorod array was obtained, which is several times higher than that of the Au nanorod array.

©2009 Optical Society of America

OCIS codes: (110.3010) Image reconstruction techniques; (240.6680) Surface plasmons; (130.2790) Guided waves; (230.3990) Micro-optical devices

References and links

1. J. B. Pendry, "Negative refraction makes a perfect lens," *Phys. Rev. Lett.* **85**, 3966-3969 (2000).
2. N. Fang, H. Lee, C. Sun, and X. Zhang, "Sub-diffraction-limited optical imaging with a silver superlens," *Science* **308**, 534-537 (2005).
3. D. O. S. Melville and R. J. Blaikie, "Super-resolution imaging through a planar silver layer," *Opt. Express* **13**, 2127-2134 (2005), <http://www.opticsinfobase.org/oe/abstract.cfm?URI=oe-13-6-2127>.
4. B. Wood, J. B. Pendry, and D. P. Tsai, "Directed subwavelength imaging using a layered metal-dielectric system," *Phys. Rev. B* **74**, 115116 (2006).
5. Z. Jacob, L. V. Alekseyev, and E. Narimanov, "Optical hyperlens: Far-field imaging beyond the diffraction limit," *Opt. Express* **14**, 8247-8256 (2006), <http://www.opticsinfobase.org/oe/abstract.cfm?URI=oe-14-18-8247>.
6. A. Salandrino and N. Engheta, "Far-field subdiffraction optical microscopy using metamaterial crystals: Theory and simulations," *Phys. Rev. B* **74**, 075103 (2006).
7. I. I. Smolyaninov, Y. Hung, and C. C. Davis, "Magnifying superlens in the visible frequency range," *Science* **315**, 1699-1701 (2007).
8. Z. Liu, H. Lee, Y. Xiong, C. Sun, and X. Zhang, "Far-field optical hyperlens magnifying sub-diffraction-limited objects," *Science* **315**, 1686 (2007).
9. A. Ono, J. Kato, and S. Kawata, "Subwavelength optical imaging through a metallic nanorod array," *Phys. Rev. Lett.* **95**, 267407 (2005).
10. G. Shvets, S. Trendafilov, J. B. Pendry, and A. Sarychev, "Guiding, focusing, and sensing on the subwavelength scale using metallic wire arrays," *Phys. Rev. Lett.* **99**, 053903 (2007).
11. S. Kawata, A. Ono, and P. Verma, "Subwavelength colour imaging with a metallic nanolens," *Nature Photonics* **2**, 438-442 (2008).
12. R. Zia, M. D. Selker, P. B. Catrysse, and M. L. Brongersma, "Geometries and materials for subwavelength surface plasmon modes," *J. Opt. Soc. Am. A* **21**, 2442-2446 (2004).
13. Y. Kurokawa and H. T. Miyazaki, "Metal-insulator-metal plasmon nanocavities: Analysis of optical properties," *Phys. Rev. B* **75**, 035411 (2007).
14. G. Veronis and S. Fan, "Modes of subwavelength plasmonic slot waveguides," *J. Lightwave Technol.* **25**, 2511-2521 (2007).
15. K. S. Kunz and R. J. Luebbers, *The finite difference time domain method for electromagnetics* (CRC Press, Boca Raton, 1993), Chap. 8.
16. P. B. Johnson and R. W. Christy, "Optical constants of the noble metals," *Phys. Rev. B* **6**, 4370-4379 (1972).
17. E. S. Kooij and B. Poelsema, "Shape and size effects in the optical properties of metallic nanorods," *Phys. Chem. Chem. Phys.* **8**, 3349-3357 (2006).
18. E. N. Economou, "Surface plasmons in thin films," *Phys. Rev.* **182**, 539-554 (1969).
19. S. I. Bozhevolnyi and T. Søndergaard, "General properties of slow-plasmon resonant nanostructures: nano-antennas and resonators," *Opt. Express* **15**, 10869-10877 (2007), <http://www.opticsinfobase.org/oe/abstract.cfm?URI=oe-15-17-10869>.

20. H. T. Miyazaki and Y. Kurokawa, "Squeezing visible light waves into a 3-nm-thick and 55-nm-long plasmon cavity," *Phys. Rev. Lett.* **96**, 097401 (2006).
 21. J. Le Perche, P. Quémerais, A. Barbara, and T. López-Ríos, "Why metallic surfaces with grooves a few nanometers deep and wide may strongly absorb visible light," *Phys. Rev. Lett.* **100**, 066408 (2008).
 22. E. Feigenbaum and M. Orenstein, "Modeling of complementary (void) plasmon waveguiding," *J. Lightwave Technol.* **25**, 2547-2562 (2007).
 23. G. Sauer, G. Brehm, S. Schneider, H. Graener, G. Seifert, K. Nielsch, J. Choi, P. Göring, U. Gösele, P. Miclea, and R. B. Wehrspohn, "In situ surface-enhanced Raman spectroscopy of monodisperse silver nanowire arrays," *J. Appl. Phys.* **97**, 024308 (2005).
 24. J. Yao, J. Tang, D. Wu, D. Sun, K. Xue, B. Ren, B. Mao, and Z. Tian, "Surface enhanced Raman scattering from transition metal nano-wire array and the theoretical consideration," *Surf. Sci.* **514**, 108-116 (2002).
-

1. Introduction

The resolution limitation on the order of the wavelength is always a serious restriction in conventional optical imaging, which is because the high spatial frequency components emitting from the object decay exponentially and cannot contribute to the imaging. In recent years, researchers have made some progress in preserving the evanescent components to achieve subwavelength imaging. Pendry proposed that a slab of negative refractive index material can act as a so-called superlens and suggested a practical scheme at optical frequencies such as utilizing a planar silver film in the near field condition, for which only a negative permittivity is necessary [1]. This scheme was experimentally demonstrated soon after [2,3]. Another development is the proposal of a kind of anisotropic metamaterial, which has a structure of alternating layers with permittivity of opposite signs and a hyperbolic dispersion. The superlens of this metamaterial can not only transmit the evanescent wave but also magnify the image to be resolved by the conventional optical microscope if the surface of the superlens is curved [4-6]. Experiments based on this proposal at optical frequencies were also reported lately [7,8]. In these experiments, both the silver film and metamaterial superlenses are dependent on the negative permittivity of the metal at the optical frequency and can be understood as based on the surface plasmon (SP) resonance with the evanescent wave on the surface of the metal layer [2,4,7].

Besides the above mentioned superlenses, another approach of subwavelength imaging has been proposed [9-11], which is using metal nanorod arrays to transfer the near-field information of the object point by point from one end to the other of each nanorod. The transmission of the evanescent wave is based on the surface plasmon resonance along the metal nanorods. Furthermore, if an array is arranged tapered, it can also realize image magnification [10,11].

For the nanorod array imaging, the resolution, i.e. the pitch of the array, is limited by the electromagnetic field distribution outside the nanorods, which will cause the coupling between them if they are too close. So to obtain a higher resolution, the field extent of a rod must be reduced. For this purpose, here we propose a kind of nanorods of metal-insulator-metal (MIM) structure, which are like the well known MIM slab or slot SP waveguides [12-14] but different at aspects that the width of the waveguide and the thickness of the metal layers are limited. The MIM nanorods are expected to have the same ability as the MIM slab or slot waveguides that confining most of the electromagnetic field in the insulator core with only a small fraction distributing outside. Then arrays composed of MIM nanorods could be used to improve the resolution for subwavelength imaging. In this paper, we numerically investigated the SP modes and field distribution of a single MIM nanorod and coupling between two nanorods. Subsequently, the imaging property of the MIM nanorod array was presented. At the same time, metal nanorods and metal nanorod arrays were investigated for comparison. The finite-difference time-domain (FDTD) method [15] was employed for the calculations. The results indicate that the resolution can be improved several times with the MIM nanorod array.

2. Field distribution of one nanorod and coupling between two nanorods

The transverse cross sections of a MIM nanorod and a metal nanorod are shown in Fig. 1. In Fig. 1(a), one 5-nm-thick SiO₂ layer is sandwiched between two 10-nm-thick Au layers. With the width of 25 nm, they form a square cross section. The Au nanorod in Fig. 1(b) has the same square cross section as the MIM nanorod with the side length of 25 nm. The dielectric surrounding the rod is assumed as vacuum in this work. We set the axes as in the figures: the z axis is along the central line of the rod and the x axis perpendicular to the upper side of the rod. In the calculation, the unit cell sizes are 1×2.5×2.5 nm³ and 2.5×2.5×2.5 nm³ for the MIM rod and Au rod, respectively. The dielectric constant of SiO₂ is set as 2.25 and Au is set as a Drude model [15] $\varepsilon(\omega)=\varepsilon_{\infty}+(\varepsilon_s-\varepsilon_{\infty})/(1-i\omega\tau)+i\sigma/(\varepsilon_0\omega)$, where ε_0 is the vacuum permittivity, ε_{∞} is infinite frequency permittivity, ε_s is static permittivity, τ is relaxation time, and σ is conductivity. The values $\varepsilon_{\infty}=7.9553$, $\varepsilon_s=-15019$, $\tau=9.1744\times 10^{-15}$ s, and $\sigma=1.4503\times 10^7$ S/m are obtained from fitting to the experimental bulk dielectric constant of Au [16] for the range of 700-1100 nm. It should be mentioned that the physical meaning of the parameters are not important provided that the dielectric constant given by the formula is correct. The actual dielectric constant of Au may be a little different from the bulk one because the transverse sizes of the Au layers are comparable to the electron mean free path of Au [17], but this will not result in any substantial effects on the results.

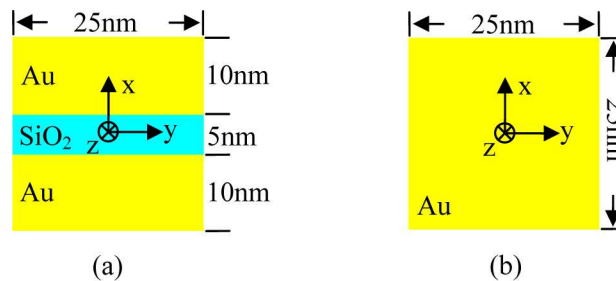


Fig. 1. Geometries of the transverse cross sections of the (a) Au-SiO₂-Au nanorod and (b) Au nanorod.

There are two SP modes of the MIM nanorod: symmetric and antisymmetric mode. Here the “symmetric” and “antisymmetric” are consistent with the definition for the MIM slab waveguide [13], which means the symmetry of the electric field component E_x with respect to the y-z plane. For the antisymmetric mode, the field distributes mainly outside the rod [14], not conforming to our requirement. In this work, we only consider the symmetric mode of the MIM rod. Figure 2 shows the excitation of a single MIM rod and a single Au rod. The source is a electric dipole located on the central line and 5 nm away from the left end of the rod at a free-space excitation wavelength of 830 nm, which is an FDTD mesh edge connected with a 1-Ampere current source at optical frequency and a 50-Ω resistance in parallel. There is no feedback of the excited modes of the nanorods to the dipoles. The dipole is x-polarized for the MIM rod to excite the symmetric mode or z-polarized for the Au rod as in [9]. To obtain SP resonance on the rod, the length of the rod must be an integral multiple of half wavelength of the SP. Here we have adjusted the lengths of the MIM rod and Au rod as 172.5 and 790 nm, respectively, so that there are four half SP wavelengths along the rod (forth order resonant mode) at 830 nm for both the two cases. In this paper, the electric field magnitudes shown in the figures are normalized to the electric field magnitudes at the positions where the centers of the far-ends of the nanorods is located but when the rods are absent, which are 1.02×10^4 and 7.15×10^3 V/m for MIM and Au rods cases, respectively. Figure 2(a) shows the distribution of electric field magnitude in the x-z plane of the MIM rod, which explicitly exhibits the SP standing wave of the 4th order resonance mode. Figure 2(b) shows the real-time distribution of electric field vector in the dashed rectangle in Fig. 2(a) with the arrows denoting the magnitude (logarithmic scale) and the direction, which shows the symmetry of the field.

Figures 2(c) and 2(d) are the same as Figs. 2(a) and 2(b), respectively, but for the Au rod. As predicted, for the MIM rod, the field is intensively concentrated in the SiO₂ layer. Oppositely, for the Au rod, most of the field distributes outside the rod. In practical applications, the antisymmetric mode of the MIM rod may be excited together with the symmetric mode by the near field source, but the antisymmetric mode is not resonant on the rod of the specific length for symmetric mode resonance because these two modes have different SP wavelengths. In the case of Fig. 2(a), we additionally set a z-polarized dipole at the same position with the same amplitude and frequency as the x-polarized dipole, and the result shows that the field distribution is mostly dominated by the symmetric mode.

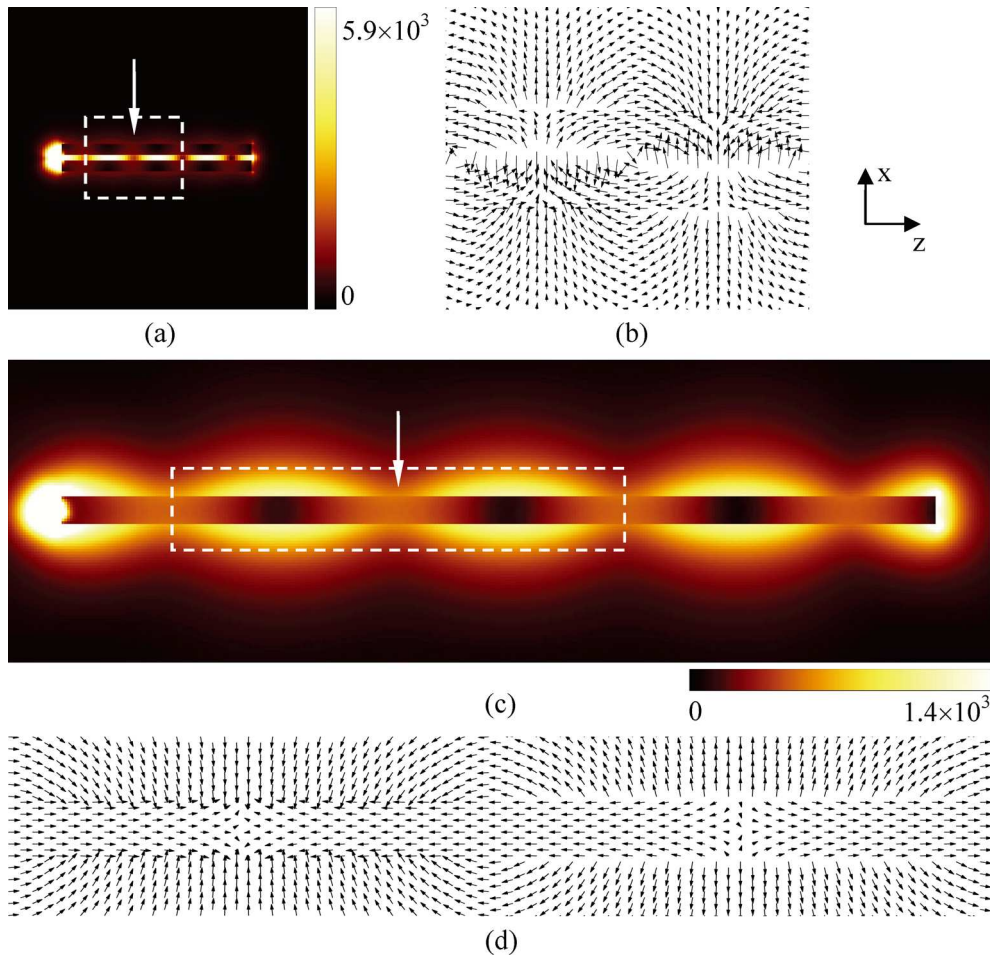


Fig. 2. (a) Distribution of electric field magnitude of the 4th order symmetric resonance mode in the x-z plane of a 172.5-nm-long MIM nanorod excited by an x-polarized dipole source on the central line and 5 nm away from the left end of the rod. (b) Real-time distribution of electric field vector in the dashed rectangle in (a) with the arrows denoting the magnitude (logarithmic scale) and the direction. (c) Same as (a) but for a 790-nm-long Au nanorod with a z-polarized dipole. (d) Same as (b) but in the dashed rectangle in (c). The arrows in (a) and (c) denote the positions of the second wave loop of the E_z standing wave of the MIM rod and Au rod, respectively.

For nanorods that are arrayed parallel to the z direction, the z component of electric field, E_z , plays a major role in the coupling between them. Figures 3(a) and 3(b) show the $|E_z|$ distributions in the cross sections at the positions of the second wave loop of the E_z standing wave of the MIM nanorod and Au nanorod, which are denoted by the arrows in Figs. 2(a) and

2(c), respectively. For the MIM rod, $|E_z|$ attains the maximum at the inner sides of the Au layers and decays away rapidly. While for the Au rod, $|E_z|$ attains the maximum at the outer sides of the rod and the decay is slower than for the MIM rod. Figure 3(c) shows the $|E_z|$ profiles on the dashed lines in Figs. 3(a) and 3(b). L1 and L3 are on the x axis and L2 is tangent to the upper side of the MIM rod. For comparison, the three curves were rescaled so that the $|E_z|$ values at the rod edges are equal to 1. For the MIM rod, the full widths at 1/e are 44 nm and 41 nm along the x and y directions, respectively. While for the Au rod, the full width at 1/e is 103 nm along each direction. We define the mode area as the product of the full widths at 1/e along the x and y directions, then the mode area of the MIM rod is 1804 nm^2 , about 1/6 of that of the Au rod, which is 10609 nm^2 . These results indicate that the ability of field confinement of the MIM nanorod is much better than that of the Au nanorod. It is also seen in Figs. 2 and 3 that the electric field enhancement of the MIM nanorod is larger than that of the Au nanorod. This can be attributed to the more intense field concentration in deep subwavelength volumes of the MIM nanorod.

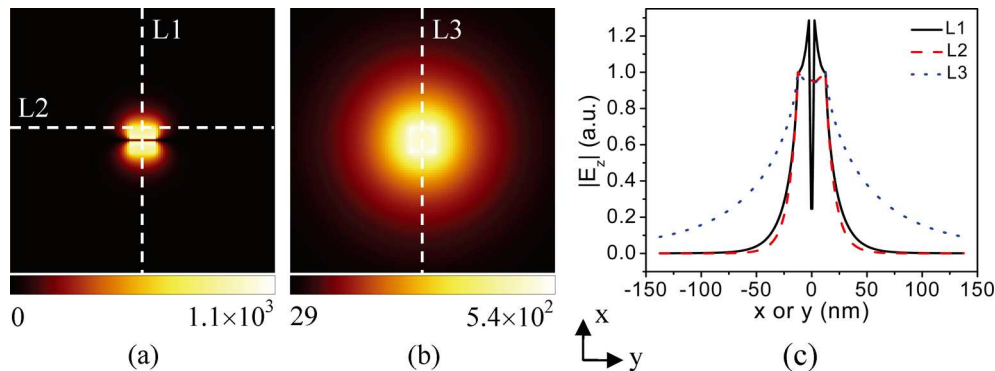


Fig. 3. (a) and (b) Distributions of $|E_z|$ in the cross sections at the positions denoted by the arrow in Figs. 2(a) and 2(c), respectively. (c) $|E_z|$ profiles on the dashed lines, L1, L2 and L3, in (a) and (b). The curves are rescaled so that the $|E_z|$ values at the rod edges are equal to 1 for comparison.

Next, we calculated the coupling between two identical nanorods when they were placed parallel. Figure 4(a) shows the distribution of electric field magnitude in the plane across the central lines of two MIM rods with only one dipole lying 5nm away from the left end of the upper rod. The corresponding top-views of the two rods on the left side denote the arrangement patterns of them and for each pattern the separation of the two rods is 20 nm. It is seen that for both patterns, seldom electromagnetic energy is coupled from the upper rod to the lower one, showing that the field at the lower rod is far weaker than at the upper one. Figure 4(b) is the same as Fig. 4(a) but for two Au rods with a separation of 120 nm. In this case the fields at the right ends of the two rods are nearly equal. Obviously, the coupling efficiency between the Au rods is much higher than between the MIM rods, although the rod separation of the former is 6 times as large as that of the later. This remarkable difference exactly results from the better confinement and smaller spatial extent of the field of the MIM structure.

3. Subwavelength imaging through MIM nanorod arrays

Based on the above analysis, arrays of periodically arranged nanorods were formed and their imaging properties were investigated. Figure 5(a) shows the configuration of a MIM nanorod array. The arrangement is tetragonal, for the cross section of the rod is square, with a pitch of 45 nm. The point sources are located under the array shaped as the letter “P” and each one is on the central line of a rod. All the point sources are x-polarized and in phase. Here the point sources are set coherent since lasers are the usual light sources in most applications. Figures 5(b)-5(e) show intensity distributions in four planes perpendicular to the z axis, which are the

bottom and the top cross sections of the array, the ones 10 nm and 20 nm above the array, respectively. In the first three planes, the shape of “P” is maintained point by point, although it becomes distorted in the fourth plane. Therefore, the image formed by the point sources is transferred through the array from its bottom to its top. We also show the intensity distributions in the cross sections at the top of and 10 nm above two MIM nanorod arrays with a 40 nm pitch and a 35 nm pitch in Figs. 5(f)-5(i), respectively, and the other parameters are as in Fig. 5(a). In the case of 40 nm pitch, even though the coupling between adjacent rods is somewhat more intense than in the case of 45 nm pitch, the image of “P” in the plane 10 nm above the array is still distinct enough. But in the case of 35 nm pitch, the coupling between adjacent rods becomes further more intense so that the image of “P” in the plane 10 nm above the array is obscured by the background and a little distorted. So we conclude that the resolution limit that the MIM nanorod array can achieve is 40 nm, which is about 1/20 of the light wavelength. For comparison, Fig. 5(j) shows the calculation result of the intensity distribution in the top cross section of an Au nanorod array with the same scheme as the MIM nanorod arrays except that the pitch is 145 nm and the dipoles are z-polarized. As can be seen, the image of “P” is no more maintained in this case. This is because the coupling between adjacent rods is so serious that the rods are not independent from each other. These results verify our expectation that the MIM nanorod array can achieve imaging with a smaller pitch than the metal nanorod array and hence realize a higher spatial resolution.

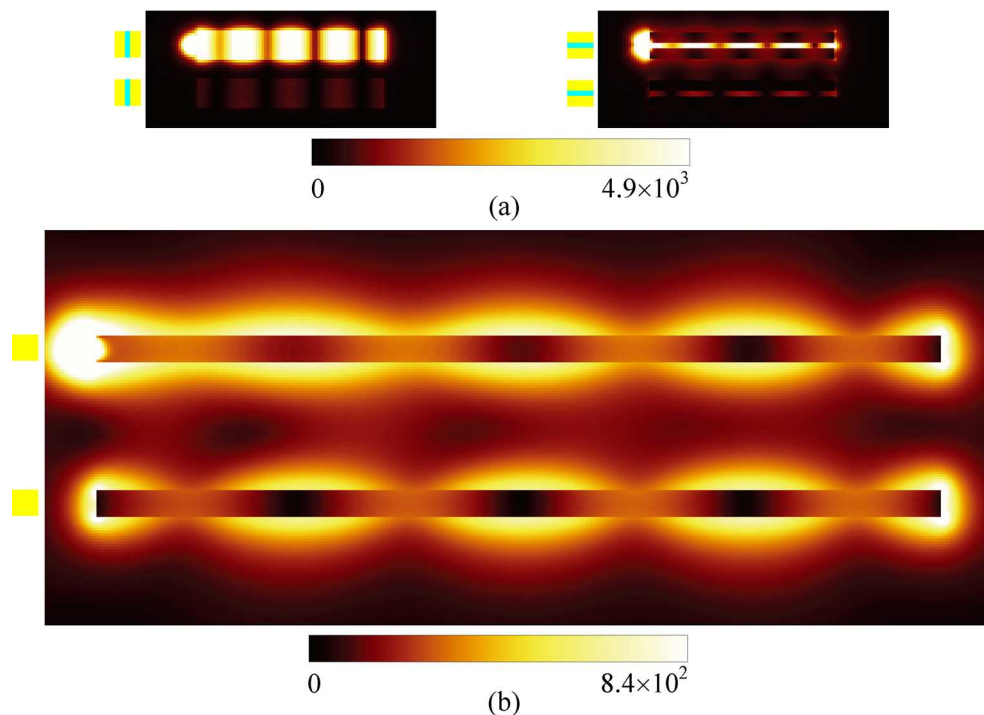


Fig. 4. Distributions of electric field magnitude of two parallel nanorods with only one dipole source located 5 nm away from the left end of the upper rod in the plane across the central lines of the two rods. The arrangement patterns are shown by the top-views of the two rods on the left side, respectively. (a) For two MIM rods with a separation of 20 nm; (b) for two Au rods with a separation of 120 nm.

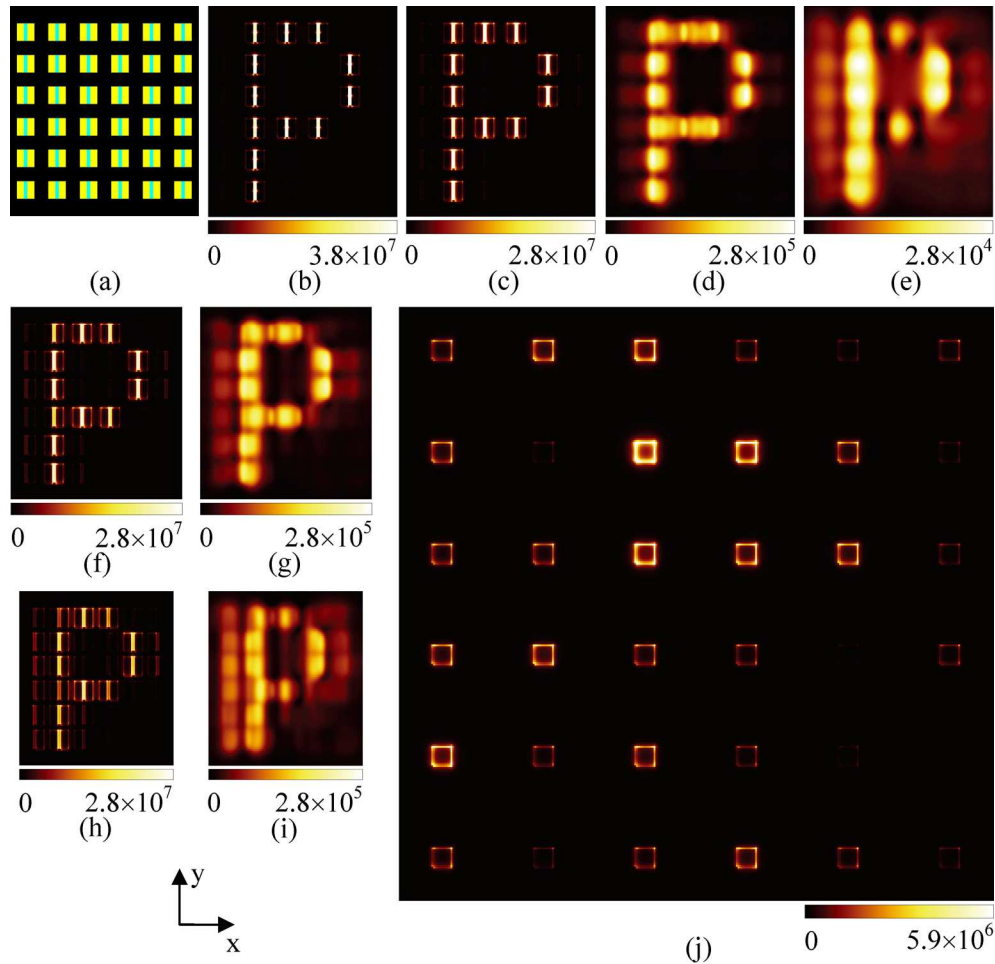


Fig. 5. Subwavelength imaging through nanorod arrays. (a) Configuration of a MIM array, which is a tetragonal arrangement with a pitch of 45 nm. Twelve x-polarized and in-phase dipoles are located 5 nm under the array with each one on the central line of a rod and shaped as the letter “P”. (b)-(e) Intensity distributions in cross sections of the array in (a), which are at the bottom and the top of the array, 10 nm and 20 nm above the array, respectively. (f)-(g) Same as (c)-(d), respectively, but with a pitch of 40 nm. (h)-(i) Same as (c)-(d), respectively, but with a pitch of 35 nm. (j) Same as (c) but for an Au nanorod array with a pitch of 145 nm and the dipoles are z-polarized.

4. Effect of variation of the MIM nanorod geometry on the SP mode

We now consider the effect of variation of the MIM nanorod geometry on the SP mode. Figures 6(a)-6(c) show the SP wavelength, the propagation length and the mode area at the free-space excitation wavelength of 830 nm as a function of the SiO₂ thickness, respectively, with other parameters as in Fig. 1(a). Like for the MIM slab [12] or slot [14] waveguide, all the three mode characteristic parameters in Figs. 6(a)-6(c) increase with increasing SiO₂ thickness. The MIM structure results in strong shortening of the SP wavelength and propagation length, i.e. the SPs become slow [18,19], which becomes crucial when the SiO₂ thickness is a few nanometers, so the MIM nanorod exhibits very strong field confinement and enhancement. This phenomenon has been experimentally demonstrated [20] and can be interpreted with the “electrostatic regime” [21,22], which is the physical origin of the high resolution of the MIM nanorod array: each nanorod behaves as if it were alone although separated by only 40 nm (see Fig. 5). The effect of varying the thickness of the Au layers was also investigated and analogous results were obtained that as the Au thickness increases, both

the propagation length and mode area increase. This indicates that a smaller mode area is always accompanied by a shorter propagation length. From the view point of practice, the thicknesses of 5 nm and 10 nm are almost the lower limits for SiO₂ layer [13] and Au layer, respectively. So the geometry in Fig. 1(a) corresponds to almost the smallest mode area that can be realized for the MIM nanorod. In this case, the propagation length is less than 0.2 μm as shown in Fig. 6(b). However, it is proposed in [11] that long distance imaging can be realized without significant loss by using a stacked arrangement of layers of unit nanorod arrays, because the imaging is via the SP resonance on the unit nanorods and the coupling between adjacent layers rather than the long distance propagation of SP along long nanorods. Obviously this approach is still valid for the MIM nanorod arrays.

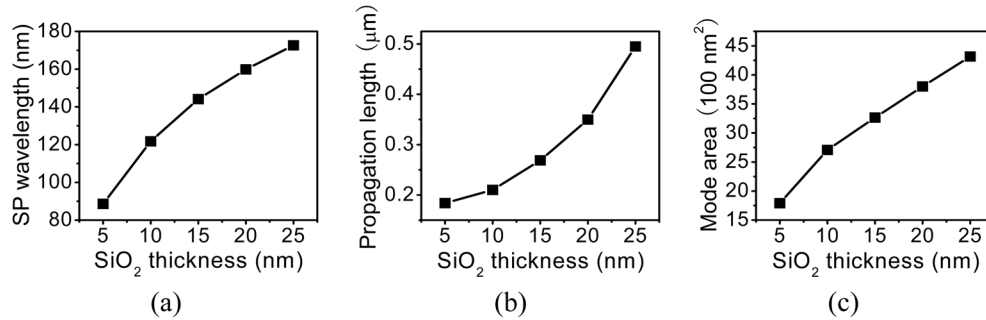


Fig. 6. (a) SP wavelength, (b) SP propagation length and (c) mode area at the free-space excitation wavelength of 830 nm versus the thickness of the SiO₂ layer with other parameters as in Fig. 1(a).

5. Conclusion

We have numerically demonstrated that the Au-SiO₂-Au nanorod confines the electromagnetic field inside the rod more effectively and has a smaller field extent than the Au nanorod. The mode area of the Au-SiO₂-Au nanorod is about 1/6 of that of the Au rod. According to the simulations of imaging through the Au-SiO₂-Au and Au nanorod arrays, for coherent light sources, the resolution limit of the Au-SiO₂-Au nanorod array, which is 40 nm ($\sim\lambda/20$), is several times smaller than that of the Au nanorod array. This exhibits the great potential of the MIM nanorod array for improving the resolution of subwavelength imaging. In addition, the large electric field enhancement of the MIM nanorod suggests the applications of the MIM nanorod array in surface enhanced Raman scattering [23,24].

Acknowledgments

This work was supported by the Program for New Century Excellent Talents in University, the National Natural Science Foundation of China under grant No. 60878021, and the National Basic Research Program of China under grant No. 2007CB307001.